

Application of the Trend Filtering Algorithm on the MACHO Database

Szulágyi, J.^{1,2}, Kovács, G.², Welch, D. L.³

¹ Eötvös University, Department of Astronomy, Budapest, P.O. Box 32, H-1518 Hungary

e-mail: szulagyi@konkoly.hu

² Konkoly Observatory, P.O. Box 67, H-1525, Budapest, Hungary

e-mail: kovacs@konkoly.hu

³ Department of Physics and Astronomy, McMaster University, Hamilton, Ontario, Canada, L8S 4M1

e-mail: welch@physics.mcmaster.ca

Received / Accepted

ABSTRACT

Aims. Due to the strong effect of systematics/trends in variable star observations, we employ the Trend Filtering Algorithm (TFA) on a subset of the MACHO database and search for variable stars.

Methods. TFA has been applied successfully in planetary transit searches, where weak, short-lasting periodic dimmings are sought in the presence of noise and various systematics (due to, e.g., imperfect flat fielding, crowding, etc). These latter effects introduce colored noise in the photometric time series that can lead to a complete miss of the signal. By using a large number of available photometric time series of a given field, TFA utilizes the fact that the same types of systematics appear in several/many time series of the same field. As a result, we fit each target time series by a (least-square-sense) optimum linear combination of templates and frequency-analyze the residuals. Once a signal is found, we reconstruct the signal by employing the full model, including the signal, systematics and noise.

Results. We apply TFA on the brightest ~5300 objects from subsets of each of the MACHO Large Magellanic Cloud fields #1 and #79. We find that the Fourier frequency analysis performed on the original data detect some 60% of the objects as trend-dominated. This figure decreases essentially to zero after using TFA. Altogether, We detect 387 variables in the two fields, 183 of which would have remained undetected without using TFA. Where possible, we give preliminary classification of the variables found.

Key words. methods: data analysis – stars: variables – galaxies: Magellanic Clouds

1. Introduction

Microensing survey projects initiated in the 1990s yielded unprecedented amounts of data for variable star research. Subsequent analyses and followup observations focused on certain types of variables and largely ignored the several millions additional lower-amplitude variable stars spanning the HR-diagram, including those not suspected of belonging to existing classes of stellar variability. Since then, a new class of intensive photometric survey has emerged motivated by the search for transiting extrasolar planets. Here, due to the unexpected nature of various extrasolar planets, the analysis is not restricted to a subsample of the collected time series. It quickly became evident from these surveys that the expected faint signals are usually overwhelmed by the much larger systematic effects (or trends) due to imperfect conditions, hardware and photometric data reduction. Until recently, image and photometric reduction methods were unable to retrieve the bulk of variability information in these collections of data. To cure this deficiency, methods have been developed such as the one of Kruszewski & Semeniuk (2003), SysRem by Tamuz, Mazeh & Zucker (2005) and TFA by Kovács, Bakos, & Noyes (2005, hereafter KBN) to filter out systematics in a post-processing phase. The method of Kruszewski & Semeniuk (2003) is devoted to reconstruct the signal with known period. This includes a combined fit of a Fourier series (with the signal period) and a polynomial with the hour angle. On the other hand, SysRem and TFA are capable of searching

for and reconstructing signals by using the temporal characteristics of the objects observed in the field to find the part of the target time series that comes from the systematics.

Attempts have been made to deal with the most easily identified systematics and to correct for them. For example, the method of External Parameter Decorrelation (EPD, see Bakos et al. 2009) utilizes the fact that, for constant stars, certain image properties (e.g., position, PSF width and elongation) correlate with the brightness deviations from the average value. There is also the method of Differential Image Analysis (DIA, see Alard & Lupton 1998 and for a summary Bramich 2008) that has been used very successfully in variable star searches over the past ten years. None of these methods result in photometric time series that are completely free of systematics. This is because they use only the spatial information on the images and do not include the temporal information, which is available in great abundance from long-term observations.

We briefly describe our method in Sect. 2. In Sect. 3, for the preparation of the data analysis, we perform various tests to optimize our search for variables in Sect. 4. Discussion and summary of the results are given in Sect. 5.

2. The trend filtering method

The various aspects of the trend filtering method has already been described in several other papers (e.g., KBN, Kovács &

Bakos 2008). Here we briefly summarize the basic steps and encourage the reader to consult with those papers for more details.

The basic idea behind TFA is that any systematics (or trends – we use these terms interchangeably) contaminating the target signal can be linearly decomposed with the aid of some subset of the photometric signals (or light curves, LCs for simplicity) of the objects observed in the given field. This template lightcurve set is expected to show the various types of brightness variations which are common in many stars (constant or variable) in the field. There are two steps in the analysis:

- Assuming that the target signal is trend- and noise-dominated, we fit the target signal by the linear combination of a pre-selected template LC set. This fit yields a residual time series that is supposedly trend-free and contains only the signal (with some distortion – see below) and noise, that is nearly white (compared to the starting noise spectrum). This filtered time series is frequency-analyzed and searched for dominant frequency components.
- Once the frequencies are found, one may want to *restore* the signal, since in the above procedure we assumed that there are only systematics and noise. Since some part of the original signal may have been fitted and subsequently subtracted (unintentionally) from the original time series, we need to restore the signal by employing a *full* model that contains the *signal+trend+noise*. Once the constituting frequency components are known, we can perform this reconstruction by iteratively approximating the signal and trend part of the observed signal. For periodic signals the method has been described in KBN, for multiperiodic ones we refer to Kovács & Bakos (2008).

We note the following. The template set is selected in a nearly uniform (X, Y) grid covering the full field. This distribution of templates makes the selection of close pairs fairly unlikely, thereby decreasing the chance of eliminating blended variables that could be further studied by other means (e.g., by large-telescope followup observations). A lower brightness limit is also set, since very faint targets are dominated mostly by random noise and therefore are less valuable for trend filtering (see however Mazeh, Tamuz & Zucker 2007 for possible systematics in faint stars). We do not omit variables from the template, because: (i) variables are relatively rare (e.g., some 5% of the Galactic field stars are variable – see Kovács & Bakos 2008); (ii) we do not know *a priori* which stars are variable and; (iii) we do not generate additional signal in the target time series by including variables in the template set (see KBN for the discussion of the effect of a template with sinusoidal variation on a target of pure noise).

For time series of limited number of data points, large numbers of template (comparable with the number of data points) will generate correlated noise in the filtered time series. Although this is a general feature of any type of data fitting, the effect is still likely to be tolerable when compared with the level of correlation caused by the systematics in the original time series. To avoid over-fitting, we compute the unbiased estimate of the standard deviation of the residuals and select a template number for which this standard deviation starts to level off. As an additional test we also show the insufficiency of the use of a single, but optimally selected template as a substitute of multiple templates (see Sect. 3.2).

The multiple spatial template requirement is consistent with the manner in which the photometry in the MACHO Project database was originally reduced. Alcock et al (1999) describe reduction and calibration of the MACHO Project photometry,

noting that each image was broken into 512×512 pixel subimages for separate, parallel-efficient reduction. Furthermore, a focal plane-wide pattern of zero point residuals was found, likely due to variations in the large, dichroic beamsplitter.

3. Preparation of the analysis

Before applying TFA on MACHO photometry, it is important to investigate the basic properties of the data, because we would like to use the method in an optimum way, by filtering out systematics at the lowest possible filter order (i.e., template number N_{TFA}).

Because our earlier experiments with the HATNet¹ data show that fairly large number of templates (in the order of several hundred, see KBN) are necessary to reach the desired white noise level, we needed to investigate this issue in the particular case of MACHO time series photometry in order to avoid overfitting the data.

In Sect. 3.1 we describe the data used in this paper. Sect. 3.2 is devoted to several tests, including those of finding the optimum template number, demonstrating the improvement in the distribution of the frequencies of the main harmonic components of the TFA time series and showing the inadequacy of best single template fit. We also give an estimate on the false alarm level based on Gaussian time series simulations.

3.1. The data

We selected sub-samples from two neighboring LMC fields (#1 and #79) to create sample databases containing some 5300 stars from the bright tail of the magnitude distribution of each field. Field #79 is densely populated at the Northern edge of the LMC bar, containing altogether 532264 objects. In practice, a MACHO Project “object” is a defined location in the focal plane where a sum of a small number of images with better-than average image quality exceed the threshold of a the star-finding algorithm. An object may constitute a single star but also may be the combined light of several stars in a single MACHO Project resolving element.

Field #1 overlaps #79 and is situated further west at the end of the bar of the LMC. This is a somewhat sparser field with 503227 objects detected by the MACHO survey. Both datasets cover a long and continuous time interval of 7.5 years, starting in 1992. We use the MACHO “b” instrumental magnitudes, because of the better noise characteristics based on our earlier works on RR Lyrae stars (Alcock et al. 2003).

To check the unbiased nature of our samples in terms of colors (and implicitly physical properties), we plot the color-magnitude diagrams (CMDs) in Fig. 1. To limit the sample size and exclude too many noisy targets but at the same time to reach the overall luminosity level of the RR Lyrae stars, we applied a cut at $V = 20$ mag.

The transformation of the instrumental magnitudes to the (Cousins) R and (Johnson) V magnitudes have been discussed by Alcock et al. (1999). Here we use the formulae given by Alcock et al. (1997) for the LMC (their Eq. (1)). The figure shows that the sample used in our analysis covers the expected full color range of objects observed by the project (see the CMD of Alves et al. 1999 for nine million objects from the LMC).

Because TFA requires exactly the same set of observation epochs for all LCs, it is important to check how well this uni-

¹ Hungarian-made Automated Telescope Network, see <http://cfa-www.harvard.edu/~gbakos/HAT/>

form sampling condition is satisfied. Figure 2 shows the distribution of the number of data points on each LC. As expected, #79 displays a different distribution, because of the more frequent observations of the LMC bar field. It is important to note that 80% of the objects have number of photometric measurements in the ranges of 1180–1250 and 1460–1550 for #1 and #79, respectively. All stars in the TFA template sets are brighter than $V = 18.6$ mag and none of the objects in either fields in the above samples have fewer than 1000 data points (objects containing fewer data points were not selected – we see from the figures that this cut is justified). This allows the application of TFA on all stars, with some special attention to be paid to the low- N cases, when the empty values are to be filled in by the average of the time series. We note that this necessary extension of the target time series has little effect on the final result, because: (i) there are only a few stars with significantly fewer data points than the average; (ii) we use a common sampling time base only for frequency search; (iii) the final result (i.e., the reconstructed LC) is based on “target-adapted” data points, i.e., we sample the templates on the time base of the target.

It is also useful to check the distribution of the standard deviations, since selection of outliers and other processes affecting the final data quality depend on this quantity. Figure 3 shows that both fields have similar error distributions, perhaps with a slight surplus of objects with errors larger than ~ 0.2 mag in field #79. This suspected difference can be attributed to the $\sim 6\%$ higher surface density of objects in #79 relative to #1. We note that in the analyses presented in this paper we employ a fairly liberal upper limit of 0.4 mag for selecting erroneous data points based on the errors derived from the images by the MACHO pipeline. In addition, further data points are discarded by an iterative 5σ -clipping based on the standard deviation of the time series. The overall value of the standard deviations of the TFA-filtered LCs toward the faint limit of $V = 19.0$ mag is about 0.15 mag. In assessing the minimum detectable amplitude in this regime, we assume that the stars are mostly dominated by white noise. From the approximate $A/(\sigma\sqrt{2/N}) > 7$ condition (valid in the high SNR limit – see, e.g., Kovács 1980), for field #79 with an average number of data points of $N = 1400$ we get a 7σ lower limit of ~ 0.04 mag for the amplitudes of periodic signals detectable even toward this faint end of our sample.

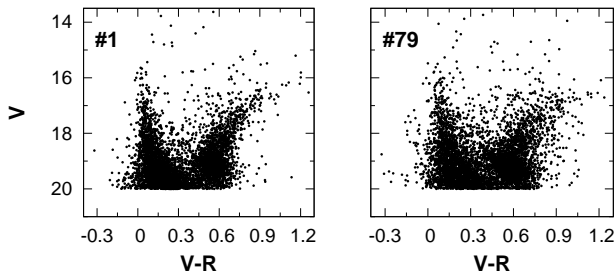


Fig. 1. Color-magnitude diagrams for the stars analyzed in this paper in the LMC fields #1 and #79. Data were cut at $V = 20$ mag.

3.2. Tests for optimum analysis

First we check the TFA template number (N_{TFA}) dependence of σ_{TFA} , the unbiased estimate of the standard deviation of the residuals remaining after subtracting the systematics from the

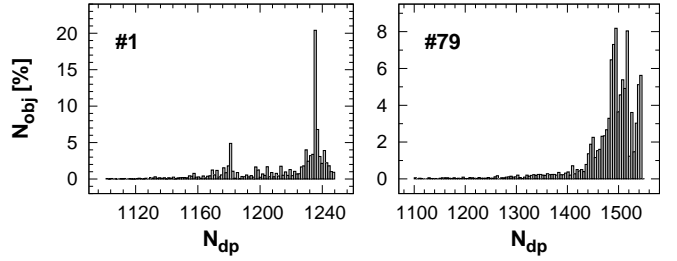


Fig. 2. Distribution of the number of the constituting data points of the light curves of the stars analyzed in this paper in the LMC fields #1 and #79.

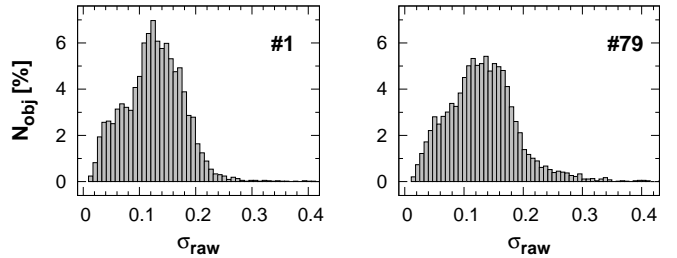


Fig. 3. Distribution of the standard deviations of the light curves analyzed in this paper from the LMC fields #1 and #79.

original time series. Omitting the further decrease of the standard deviation due to signal reconstruction is reasonably justified, since less than 5% of the stars are variables, where reconstruction really matters. The unbiased estimate is computed as given in Appendix A.

Figure 4 shows the variation of σ_{TFA} for 100 randomly selected stars from each field, exhibiting integer d^{-1} systematics. For comparison, we also plot the results obtained on pure Gaussian white noise data generated on the time base of the same stars. We see a clear decrease of σ_{TFA} with the increase of N_{TFA} for the observed data. The expected constant level of the test data is also well exhibited. From the individual results (thin lines) we see that there are fairly large differences among the various objects in respect of the run of σ_{TFA} . For ‘well-behaved’ systematics and extensive data sets we expect a steadily decreasing σ_{TFA} from low template numbers to some optimum value and then leveling off to a basically constant value. This pattern is approximately present only in a few cases. In general, we see a nearly monotonic decrease of σ_{TFA} all through the template numbers tested. We suspect that this behavior is related to the large variety of systematics that are still not possible to catch even with the largest number of templates tested. In any case, based on the above test and the one described below, as a compromise between overall data number and trend filtering level, we fix the template number to 600 and 500 for fields #79 and #1, respectively.

In a subsequent test we show that the above choice of template number is adequate for filtering out prominent systematics. We follow KBN, where the filtering capability was tested by the comparison of the occurrence rates of the peak frequencies found by the Box-fitting Least Squares (BLS) analysis (see Kovács, Zucker & Mazeh 2002) before and after the application of TFA. Here we perform the same type of test but we use Discrete Fourier Transformation (DFT, see e.g., Deeming 1975), since we are mostly interested in the oscillation compo-

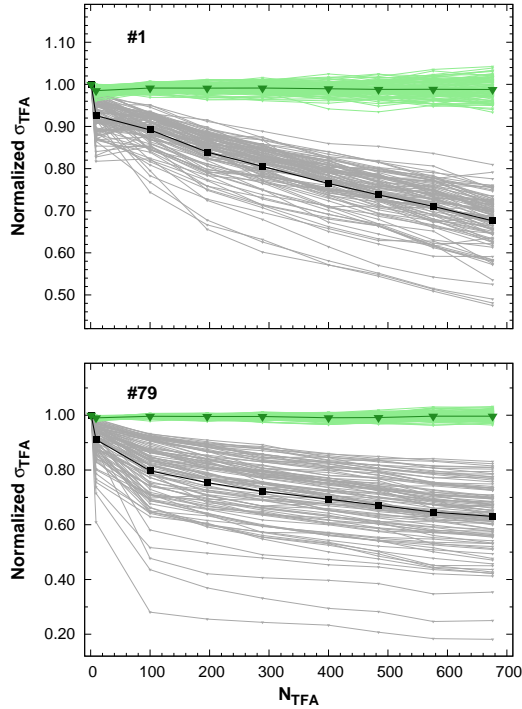


Fig. 4. Dependence of σ_{TFA} (see Appendix A) on N_{TFA} . Near horizontal lines are for pure white noise test data. Thin lines are for the individual objects. Thick lines show the average values computed from the 100 objects. Each function is normalized to 1.0 at $N_{\text{TFA}} = 0$, i.e., for the standard deviation of the original (non-TFAd) data.

nents of the data. The resulting distribution functions are shown in Figs. 5 and 6. We see that the original (RAW) data exhibit very strong systematics associated with various forms of the common $1d^{-1}$ effects (e.g., change in the point spread function, color-dependent absorption, etc.). All of these are absent in the TFA-filtered data and the frequency distributions are nearly flat, as expected from a randomly selected sample of stars. At the low-frequency end, a part of the remaining objects are real (long-period) variables as we are to discuss them in Sect. 4. In addition to the cyclic systematics, TFA is capable to handle also outlier data points that originate from various transients (e.g., from non-properly subtracted cosmic rays). This property is obviously not exhibited in Figs. 5 and 6, but can be seen in several phase-folded light curves (in Sect. 4 we show an example on this).

The way TFA is currently implemented is not optimal. We select a rather large sample of templates that are used for all targets in the field. Since we do not know a priori which template members are ‘valuable’ we need to select a sufficiently large set in order to be more confident that the necessary templates for any given target are included. In keeping the ‘most relevant’ templates (or the linear combinations of those) some addition selection could be incorporated by using principal component decomposition, similarly to that of the SysRem algorithm of Tamuz et al. (2005). However, applying this or any other similar method, we have to make the decision of where to cut the main principal components. It may happen that certain systematics (e.g., transients) will escape our attention, since they will not enter in the main principal components, because the statistics we use (e.g., the eigenvalues) in the cut may not be sensitive to the given sys-

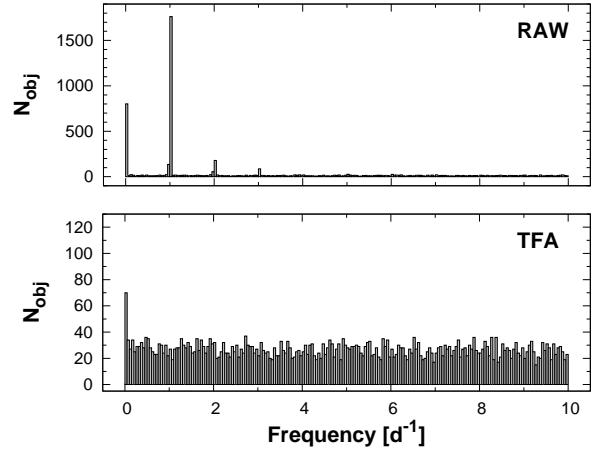


Fig. 5. Distribution of the peak frequencies for the full sample of ~ 5300 objects in field #1. The DFT analysis was performed in the frequency range of $[0.0, 10.0]d^{-1}$. Upper panel: original (RAW, non-TFAd) data, lower panel: TFAd data with $N_{\text{TFA}} = 500$.

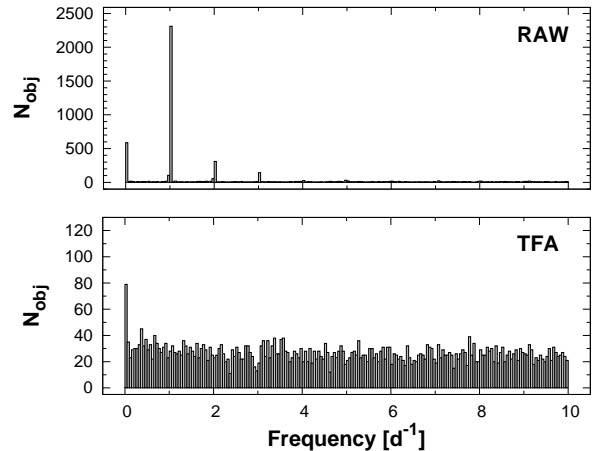


Fig. 6. As in Fig. 5, but for field #79. The TFAd data were obtained with $N_{\text{TFA}} = 600$.

tematics due to their relatively low incidence rates, low amplitudes or short durations.

In another effort to identify a more economical selection of templates, we test if the best fitting single template selected from the standard TFA template set gives similar result to the algorithm used in the original framework devised by KBN. By using the large template sets chosen above in this section, we compute the unbiased estimates of the standard deviations (see Appendix A) for all stars in the two fields. Then, for each object, we select that single-template which yields the lowest σ_{TFA} value. In Fig. 7 we plot ratio of these standard deviations versus the standard deviations computed within the original framework of KBN. It is clear that the optimum single-template selection *always performs less effectively* than the standard multi-template method. There is a dependence of the gain of the multiple template implementation of TFA as a function of the LC scatter. This effect is due to the increase of random noise of the light curves that cannot be filtered out by TFA. We also note that although the peak frequency distribution for the above optimum single-template fit is similar to that of the RAW data, there is a visible decrease in

the number of stars with integer d^{-1} frequencies. These all show that the multi-template implementation of TFA performs significantly better than its optimized single-template variant.

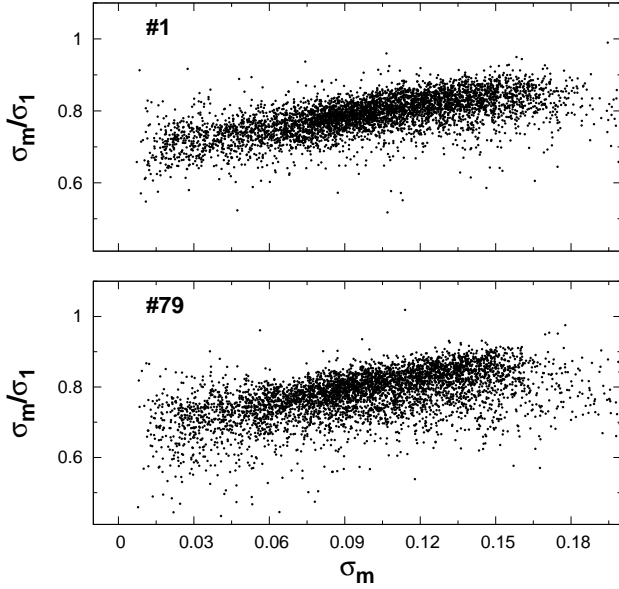


Fig. 7. Unbiased estimates of the standard deviations obtained in the multi-template (σ_m) and optimum single-template (σ_1) applications of TFA.

It is important to test the signal-to-noise ratio (SNR) above which one can declare a signal as a significant detection. Although the statistical properties of DFT on continuously sampled data are well known (e.g., Foster 1996 and references therein), for gapped and randomly sampled datasets the situation could be more complicated. Therefore, we estimate the confidence level by following the same method as in Nagy & Kovács (2006). Over a thousand time series were generated by using pure Gaussian white noise on the time base of randomly selected objects in each field. Then, these time series were treated in the same way as the real observational data and TFA/DFT analyses were performed in the $[0.0, 10.0]d^{-1}$ frequency range (with 500 and 600 templates in fields #1 and #79, respectively). After finding the peak frequency, we compute the signal-to-noise ratio, defined as follows

$$\text{SNR} = \frac{A_{\text{peak}} - \langle A_{\nu} \rangle}{\sigma_{A_{\nu}}} . \quad (1)$$

Here A_{peak} is the amplitude at the highest peak in the spectrum, $\langle A_{\nu} \rangle$ is the average (over the frequency values $\{\nu\}$ of the spectrum in the passband of the analysis) and $\sigma_{A_{\nu}}$ is its standard deviation, computed by an iterative 5σ clipping. We note that, as it follows from the above definition, for colored noise, SNR is a function of the frequency range of analysis. In the most common situation of decaying low-frequency noise (the so-called “red noise” – see, e.g., Pont et al. 2006), by increasing the frequency range, SNR also increases. Here we assume that in the frequency interval used, the data are well-filtered from systematics (corresponding to the main source of red noise) and the flat (white) noise spectra generated in the simulations represent the real distribution closely enough.

The distribution functions of the so-obtained SNR values are displayed in Fig. 8. It is remarkable that the pattern of the false alarm probability (FAP) is very similar for both fields (the small differences can be attributed to the finite sample size). Based on this diagram, we place our cutoff value at $\text{SNR} = 7.0$, corresponding to $\sim 1\%$ FAP. Although this limit might suggest a rather low rate of false detection, in practice the rate of rejected detections is much higher, because visual inspection and other criteria (e.g., blend situation) can reveal additional signatures of false detection. As a result, from the originally selected 450 variables satisfying the $\text{SNR} > 7.0$ criterion only slightly greater than 80% survived and entered our variable list. Decreasing the SNR cutoff to 6.5 we would select 1015 variables, with an estimated very large real false alarm rate, since the formal rate is already $\sim 4\%$ at this SNR value. On the other hand, a more stringent criterion of $\text{SNR} > 7.5$ would have led to the loss of some of the interesting variables, because this criterion would have been satisfied only by 330 objects, that is 10% lower than the number of the finally selected variables, based on the DFT analysis.

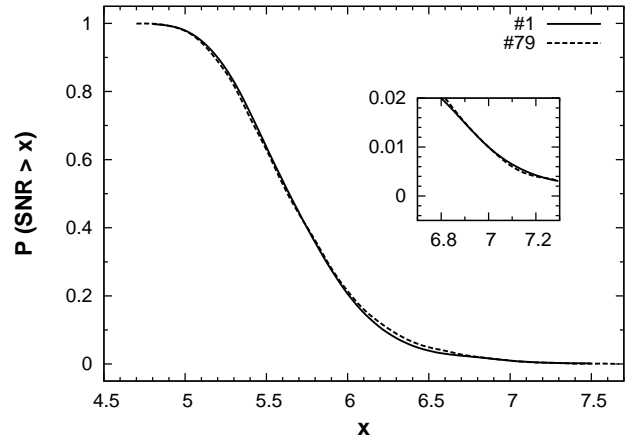


Fig. 8. False alarm probability (FAP) diagram for the data used in this paper. Inset shows the close neighborhood of the cutoff signal-to-noise ratio (SNR) of 7, above which FAP is lower than 1%.

4. Frequency analysis

We have performed DFT and BLS frequency analyses on both fields by using the optimum template numbers of 500 and 600 for fields #1 and #79, respectively. To avoid faint, noise-dominated stars, the template members were selected from stars brighter than $V = 18.6$ mag. We also performed the same analyses on the RAW data, to get an estimate on the effectiveness of TFA. The frequency bands of the searches were different for the BLS and DFT runs, since the line profiles in the BLS spectra are much narrower than those in the more traditional Fourier spectra (see Kovács et al. 2002). For the BLS analysis we took the $[0.01, 1.0] d^{-1}$ range, thereby covering most of the orbital periods of eclipsing binaries, the prime targets of the BLS search. For the DFT spectra we have a wider range of $[0.0, 10.0] d^{-1}$, since we want to cover a wide class of variables from long-period red variables to the much shorter period δ Sct stars (by covering at least those with reasonably long period to fit in the above frequency range). In both cases we used 3×10^5 frequency steps.

Variable star candidates have been selected in three main steps. First we selected targets exceeding a given SNR value

of their spectra. This cutoff value was set to 7.0 for the DFT spectra and to ~ 9 for the BLS spectra (this latter value was approximately selected on the basis of our earlier experiments that showed the BLS spectra to be more vulnerable to false alarms). In this way we selected some 200 stars from each of the two fields (many of the variables were common among the DFT and BLS candidates). Then, all variables were visually inspected and further filtered for possible false alarms. In the course of this we also assigned some preliminary classification to the variables. In the final step the independent classifications of the authors have been discussed and the final list of variable star candidates was selected. We have also performed some supplementary analyses. For example, we compared in more detail the long-period variables in the RAW and in the TFA-filtered time series and investigated the effect of target-specified time base on the signal detection (an effect that could be important in the case of targets with number of data points lower than the average). We show the coordinates and the most important parameters of the so-obtained variables in Tables 1 and 2².

We caution that our classification is *preliminary* and very *approximate*. Except for the trivial cases (e.g., typical fundamental mode RR Lyrae stars), variable star classification (i.e., the first step toward the estimation of the physical parameters) is a very difficult task in heterogeneous stellar systems. In our simple classification scheme we considered: (i) the period; (ii) the approximate brightness in V and color $V - R$; (iii) the light curve shape. These have led to 11 classes, with the wide group of long-period variables (LPVs) including objects on the AGB and beyond and, of course, miscellaneous variables, the ones that show definite variability but indefinite classification based on the parameters listed above. The broad definitions of the variable classes are as follows.

LPV : not eclipsing and period longer than ~ 10 days and brighter than the HB level of $V \sim 19$ mag

FU Cep : fundamental mode Cepheid

FO Cep : first overtone mode Cepheid

SO Cep : second overtone mode Cepheid

RRab : fundamental mode RR Lyrae

RRc : first overtone mode RR Lyrae

EB : eclipsing binaries of any type

B : \sim B-type pulsators, $V \lesssim 18.0$, $V - R \lesssim 0.1$

δ Sct : frequency is greater than $\sim 5d^{-1}$ and $0 \lesssim V - R \lesssim 0.3$

Hump : hump/eruption in the light curve

Misc : anything that cannot be classified

The following comments apply to the variable star inventories provided in Tables 1 and 2.

- Magnitudes have been derived by using Eq. (1) of Alcock et al. (1997). We note that these magnitudes are approximate and can be used only as a rough guide for variable classification.
- Variables without a dominant frequency component (leading to large – above the noise level – SNR values) will not get promoted into our lists.
- Blends are defined as those stars that have close positions and periods to those of the target but they appear to have lower SNR values (and concomitantly lower amplitudes). Except for a few cases, the distinction between the blend and the source was unique. These stars are commented together with other peculiarities in Appendix B. Blends are not reported in Tables 1 and 2.

- Frequencies can be ambiguous within integer fractions for EB stars.
- There are some near integer d^{-1} variables that may well be LPVs, but it is impossible to decide it from the present data. In particular, some of the red, short-periodic Misc variables might actually be LPVs.
- The slowly varying LPVs – those that change their brightness over the time scale of the observational time span – may be subject to “signal killing”. That is, because for long-period targets it is easier to find templates with similar long-term changes, it is also easier to subtract the signal by the proper combination of these templates. However, we checked the original (non-TFAd) LCs of all objects, and we found only a handful of them disappeared after TFA-filtering. Further examination of these cases revealed that they all had rather large scatter and variations reminiscent of systematics. Therefore, we declared them as such.
- There are some stars classified as RRab?, because the period, color and brightness are in the appropriate ranges. Otherwise the shape of the LC is not of a typical RRab and the amplitude is rather low. Similar note holds also for other types of variables.
- Although the prime selection was made on the basis of low false alarm probability, there is still some chance that a small fraction (maybe 5–10%) of the variables with low SNR are, in fact, false alarms.
- TFA detections are those with one of the following properties: (i) the RAW data show typical systematics at integer d^{-1} peak frequencies that disappear in the TFA spectra with the concomitant appearance of significant peak(s) at non-integer d^{-1} frequencies; (ii) as in (i) but the RAW frequencies are at non-integer d^{-1} frequencies. We also note that when the SNR of the TFA spectrum was higher but the RAW spectrum gave the same frequency at a lower SNR level (but above the reasonable detection limit) we considered this as a non-TFA detection.

In Table 3 we provide the statistics of the variables detected in the two fields. The large number of *exclusive* TFA detections is striking (these are the signals that did not hit the detection limit in the RAW data). Interestingly, the relative number of TFA detections in both fields is nearly the same. By applying TFA, we have *doubled* the number of detected variable stars. The variability rate (number of variables versus total number of stars analyzed) is 3–5% in the two fields, very similar to the recent rate derived from the HATNet database on selected Galactic fields (Kovács & Bakos 2008). It is also important to mention that TFA is useful even if the signal is detected already in the RAW data. If systematics are present, then signal reconstruction with the aid of TFA helps to derive more accurate signal, and eventually, more accurate stellar parameters.

To exhibit the signal detection and reconstruction power of TFA, we show three examples. In Fig. 9 we plot the DFT frequency spectra of 05011976-6921083 from field #1, a short-periodic sinusoidal variable, classified as type B (blue, relatively bright, presumably pulsating variable). The total (peak-to-peak) amplitude is only 0.03 mag in MACHO instrumental “b” pass-band. In the spectrum of the RAW data, the true signal frequency is hidden in the $1d^{-1}$ side lobe of the systematics. This component clearly stands out in the spectrum after applying TFA. Reconstruction of the signal with this period results in a substantial improvement in the noise level and in the shape of the signal (on which no assumption has been made during the reconstruction). However, it is important to note that the reconstructed sig-

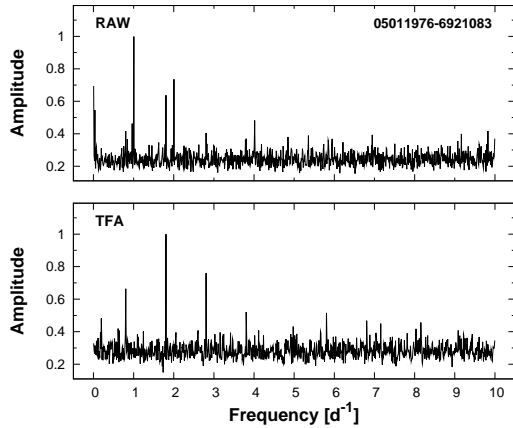
² Time series of the objects given in Tables 1 and 2 are accessible at <http://www.konkoly.hu/staff/kovacs>

Table 3. Variables in the sample of fields #1 and #79

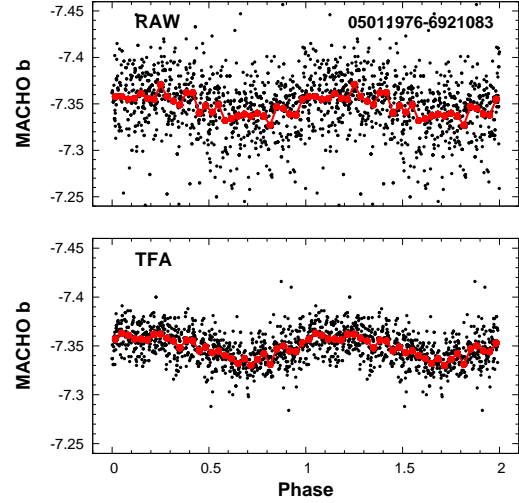
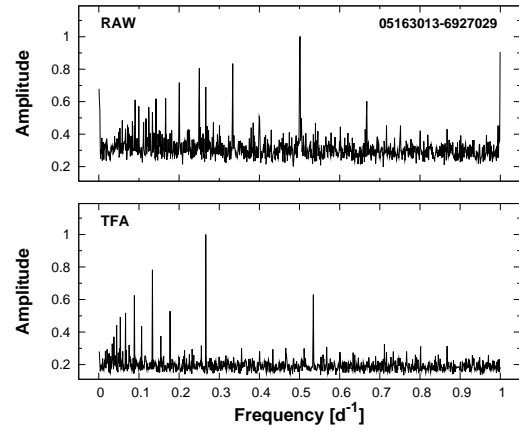
Type	#1		#79	
	ND_{RAW}	ND_{TFA}	ND_{RAW}	ND_{TFA}
LPV	18	24	34	32
FU Cep	1	1	3	0
FO Cep	3	1	0	1
SO Cep	1	1	1	0
RRab	10	4	16	3
RRc	3	3	1	1
EB	27	7	30	21
B	11	8	12	14
δ Sct	1	9	4	5
Hump	1	0	1	0
Misc	9	23	17	25
Sum	85	81	119	102

Notes: ND_{RAW} = number of detections in the original (RAW) data ND_{TFA} = number of *exclusive* detections due to TFA-filtering

nal displays the true signal with the residuals computed by the full signal model of signal+trend+noise and the latter component is simply the residual after subtracting the signal and trend components from the RAW data. Because the procedure involves the least squares fit of a considerable number of parameters, the residuals will be *biased*, i.e., they show smaller scatter as they should, due to the extra correlation generated among them by the above fit. Due to this effect (mentioned already in Sect. 3.2 and discussed in detail in Appendix A), the true noise level is some 30% higher than it is shown in the figure. Nevertheless, even with this caveat, the application of TFA clearly leads to a cleaner signal shape (which, in turn, might suggest a different classification – e.g., that of EB – but the data are insufficient to be conclusive in this case.)

**Fig. 9.** Example of the detection of a signal strongly dominated by systematics (see the high peaks at integer d^{-1} frequencies in the RAW spectrum). The variable is from field #1.

Figures 11 and 12 show a similarly strong TFA detection for the binary star 05163013-6927029 from field #79, discovered with much higher SNR by BLS than by DFT frequency analysis. The BLS frequency spectrum of the RAW data clearly shows the peak structure at $(0.5/n)d^{-1}$, reminiscence of the daily systematics present in the BLS spectra of most of the light curves. The true signal component shows up as a middle-size peak in the

**Fig. 10.** TFA reconstruction of the B-type variable shown in Fig. 9. Please check the note in the text on the scatter of the TFA-reconstructed light curve.**Fig. 11.** Example of the detection of a signal nearly completely smeared by systematics in the original (RAW) data. The frequency spectra were computed by the BLS algorithm. The variable is from field #79.

forest of the subharmonics of the daily trend. We note that the confusion in the case of BLS spectra is exaggerated due to the (sub)harmonic structure inherent to the BLS method (or to any other method, based on period-folding – see Kovács et al. 2002). The reconstructed and folded LC shown in the lower panel of Fig. 12 clearly exhibits a shallow secondary eclipse, not even suspected in the RAW LC. The bias factor for the residual scatter is the same here as mentioned in the context of Fig. 10, since for field #79 we have more data points, but, at the same time, we also have more extended TFA templates.

Our third example is devoted to demonstrate that systematics may not necessarily be exhibited in the Fourier domain. As mentioned in Sect. 3.2, transients may not always be properly subtracted from the images. Since these phenomena are non-periodic, they usually do not affect the frequency spectra in a significant way. Figure 13 shows the DFT spectra of such an object (an RR Lyrae star). The signal is easily detected already in the RAW data. Even more, we see a decrease in the SNR in the TFA spectrum. This is due to the fact that the observed sig-

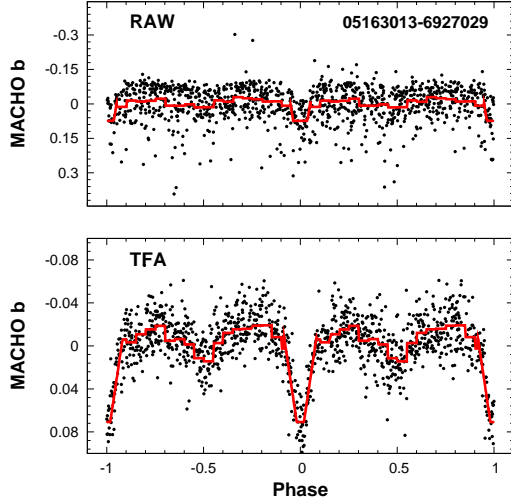


Fig. 12. TFA reconstruction of the EB variable shown in Fig. 11.

nal is strong (relative to the systematics) and in the signal search mode TFA assumes a zero target function. When this assumption is lifted, i.e. a full model is used and a signal reconstruction is made, we obtain the result shown in Fig. 14. Nearly all outlying data points are successfully corrected, with a slight accompanying change in the LC shape.

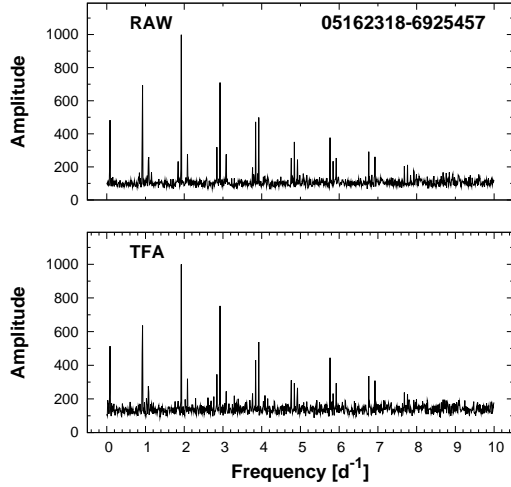


Fig. 13. Example of the detection of a DFT signal in the RAW data. The particular systematics present in this object do not affect the DFT frequency spectra. The lower frequency sidelobes visible at the alias components are due to the first harmonic (and the aliases) of the fundamental frequency. The variable is from field #79.

For a rough location of the variables in the physical parameter space, in Fig. 15 we overplot the detected variables on the CMD of #79. We see that the variables basically follow the distribution of the constant stars, with the exception of the luminous red variables and perhaps with some mild surplus of red clump variables centered at $V = 19.2$ and $V - R = 0.6$. The lack of variables on the giant branch between $V = 18$ and 17 mag is very striking. As expected from their short evolutionary life times, we do not have that many post AGB stars either. Although we have a

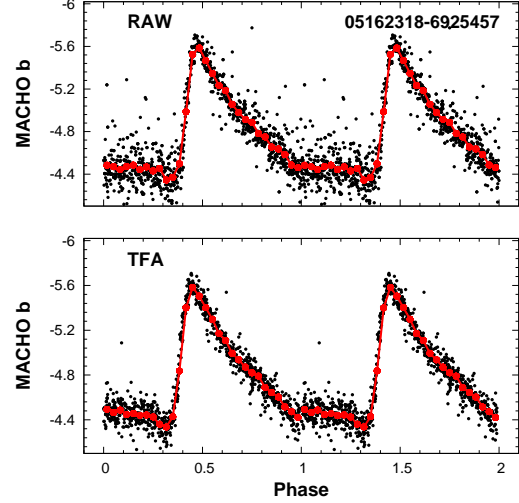


Fig. 14. TFA reconstruction of the RR Lyrae variable shown in Fig. 13. Systematics are exhibited as outlying data points, causing only a small effect on the frequency spectrum.

reasonably large number of RR Lyrae variables (41 altogether), they do not seem to form a well-defined separate group at the horizontal branch between $V = 19$ and 20 mag, but they are rather intermingled with other types of variables. On the other hand, the main sequence is nearly uniformly populated, from the the bright end down to the faintest stars in our sample.

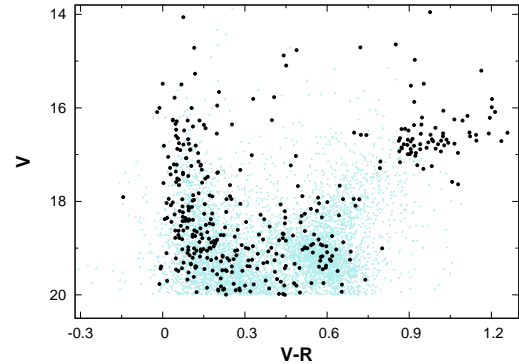


Fig. 15. Color-magnitude diagram of field #79. Overplotted are the 387 variables detected in fields #1 and #79.

5. Discussion and Conclusions

We employed the Trend Filtering Algorithm (TFA) combined with Fourier (DFT) and box-search (BLS) frequency analyses to explore the variable star content of a subset of the MACHO Project database for the Large Magellanic Cloud. From direct analyses, a large part of the database yields too many false signals due to the strong systematics present in the data. We found that about 50% of detectable variables were not detected by standard strategies in the MACHO Project database for the samples we investigated (~ 5300 objects in each of the fields #1 and #79, down to $V = 20.0$ mag). About 60% of all stars are dominated by trends.

Due to the relatively small number of data points per object, we investigated the optimum number of TFA templates to be

used in the survey. In an ideal case the representative model of a time series is reached when the increase of the number of fitting functions does not lead to a further decrease of the unbiased estimate of the standard deviation of the residuals between the input time series and the model. Unfortunately, for the MACHO Project time series, it seems that the required number of templates exceeds half of the number of data points. This would lead to a prohibitive overuse of the TFA fit and, as a result, to a significant increase in false alarms. Fortunately, the distribution of the peak frequencies of the Fourier spectra of the TFA-filtered time series – even with sub-optimal template numbers – shows that the most significant systematics exhibited as integer fractions of the diurnal periodicity disappear. We also examined the case of very long-period variables (showing basically a linear trend), where TFA is more likely to distort the light variation and lead eventually to the reduction of the true photometric variation. Although we found that the variations were real in a few cases and TFA distorted the signal considerably, visual inspections of the original (non-filtered) light curves led to the conclusion that, in general, the signals were most likely long-term systematics.

We found altogether 387 variables from the total of ~ 10600 objects analyzed in the subsets of the two fields. This variability ratio is very close to the value recently derived on a subsample of the HATNet database (Kovács & Bakos 2008). This coincidence is most probably accidental, since HATNet surveys the Galactic field stars and detects also many variables in the millimagitude amplitude regime that, for the majority of objects, is not accessible by the MACHO Project survey. Nevertheless, it is remarkable that with TFA, we are able to detect many low-amplitude variables in the few-times 10 mmag regime also in the MACHO Project database. We think that most of these variables are indeed “normal”-amplitude variables, but due to significant crowding and blending they appear as low-amplitude variables.

We find that the application of TFA in variable search increases our ability to find many low-amplitude variables that might be not accessible in the raw photometric data. This may lead to exciting new studies on various fields related to variable stars. Here we mention only three topics of immediate interest.

- Low-amplitude pulsating variables across the HR-diagram: There are of course interesting questions to raise everywhere. For example, excitation map of B-type stars is not well known, because of the delicate dependence on the metal content (Karoff et al. 2008). Limits of variability in the δ Scuti regime is still to be determined. This would be especially interesting, since linear pulsation theory predicts excitations throughout this part of the HR-diagram (e.g., Breger, Lenz, & Pamyatnykh 2008). There are regions above the Horizontal Branch (HB) still to explore: the red-clump stars, the high-metallicity, low-temperature ‘cousins’ of the HB stars; variables on the giant branch and in the AGB phase. The change of role of convection in the context of the classical κ -mechanism as we reach higher luminosity levels is not understood. The relatively well-confined instability strip of classical pulsators becomes very poorly defined at higher luminosities. Although recent investigations explored many interesting properties of the red giant variables (e.g., Soszyński et al. 2007 and references therein), they also revealed their complexity and mixed physical nature.
- Ultra low-amplitude (ULA) classical pulsators: Although the physical mechanism in establishing the borders of the instability strip of Cepheids and RR Lyrae stars is more or less known, it is still unclear how the pulsation stops and if other forms of pulsation at low amplitudes could exist out-

side the instability strip. From a subsample of the MACHO LMC Cepheids Buchler et al. (2005) found 14 objects with characteristic amplitudes of 0.005–0.01 mag. Interestingly, these stars apparently follow the PLC relation spanned by the ‘normal’ large-amplitude Cepheids. The above sample of ULA Cepheids has recently been extended by Soszyński et al. (2008). Some theoretical considerations and numerical simulations (Buchler & Kolláth 2002; Bono et al. 1995) suggest that in the case of ‘soft’ bifurcations (when the pulsation growth rates are in the same order as the evolutionary rates), the transition from various pulsation states may last several thousand years, so we may have rare, but observable events.

- Shallow-eclipsing binaries: These are important objects in extending the determination of stellar parameters toward the very low-mass ($< 0.1 M_{\odot}$) regime. Only a handful of objects span the low-mass tail of the mass–radius relation, so discovering additional objects would be very important in clarifying the source of the systematic difference between the observations and the currently available theory (Beatty et al 2007). Depending on the configuration, the depth of the eclipse can be very low, but a typical M star with an F primary yields a ~ 0.01 mag deep eclipse. It is clear that detection of such events (even if it is periodic) requires good quality data avoiding contamination with systematic effects.

Although the discovery of low-amplitude variables is a very important task, it is also a very hard one. We not only have a faint signal but it is also intermingled with the effect of colored noise due to stellar activity and instrumental systematics as discussed above. Furthermore, on the top of these, there is the blending issue. This problem has recently been highlighted by the search for extrasolar planets by transit methods (Brown & Latham 2008) and problems concerning the measured PL relations in distant galaxies (Vilardell, Jordi & Ribas 2007). The problem is quite common in all photometric works (Kiss & Bedding 2005) and can be tackled at a certain degree by various data reduction methods (i.e., image subtraction and profile analysis, see Hoekstra, Wu & Udalski 2005) but in tough cases we need combined efforts by experts on large telescope photometry, spectroscopy and stellar modeling (Mandushev et al. 2005).

Acknowledgements. This paper utilizes public domain data obtained by the MACHO Project, jointly funded by the US Department of Energy through the University of California, Lawrence Livermore National Laboratory under contract No. W-7405-Eng-48, by the National Science Foundation through the Center for Particle Astrophysics of the University of California under cooperative agreement AST-8809616, and by the Mount Stromlo and Siding Observatory, part of the Australian National University. G. K. thanks for the support of the Hungarian Scientific Research Fund (OTKA, grant No. K-60750). We are grateful to the National Information Infrastructure Development (NIIF) Program for providing CPU time for most of the computations presented in this paper (project No. 1109). DLW acknowledges the support in the form of a Discovery Grant by the Natural Sciences and Engineering Research Council of Canada (NSERC).

References

- Alard, C. & Lupton, R. H. 1998, *ApJ*, 503, 325
- Alcock, C., Allsman, R. A., Alves, D. et al. 1997, *ApJ*, 486, 697
- Alcock, C., Allsman, R. A., Alves, D. et al. 1999, *PASP*, 111, 1539
- Alcock, C., Allsman, R. A., Alves, D. et al. 2003, *ApJ*, 598, 597
- Alves, D., Basu, A., Cook, K. H. & Welch, D. L. et al. 1999, *IAU Symp.*, 190, 517
- Bakos, G. Á., Torres, G., Pál, A. et al. 2009, *ApJ*, accepted (arXiv:0901.0282)
- Beatty, T. G., Fernandez, J. M., Latham, D. W. et al. 2007, *ApJ*, 663, 573
- Bono, G., Castellani, V. & Stellingwerf, R. F. 1995, *ApJ*, 445, L145
- Bramich, D. M. 2008, *MNRAS*, 386, L77
- Breger, M., Lenz, P. & Pamyatnykh, A. A. 2008, *MNRAS*, in press (arXiv:0812.0856v1)

- Brown, T. M. & Latham, D. W., 2008, PASP, submitted (arXiv:0812.1305v1)
 Buchler, J. R. & Kolláth, Z. 2002, ApJ, 573, 324
 Buchler, J. R., Wood, P. R., Keller, S. & Soszyński, I. 2005, ApJ, 631, L151
 Deeming, T. J. 1975, Ap&SS, 36, 137
 Faccioli, L., Alcock, C. & Cook, K. 2008, ApJ, 672, 604
 Foster, G. 1996, AJ, 111, 541
 Hoekstra, H., Wu, Y. & Udalski, A. 2005, ApJ, 626, 1070
 Karoff, C., Arentoft, T., Glownienka, L. et al. 2008, MNRAS, 386, 1085
 Kiss, L. L. & Bedding, T. R. 2005, MNRAS, 358, 883
 Kovács, G. 1980, Ap&SS, 69, 485
 Kovács, G., Zucker, S. & Mazeh, T. 2002, A&A, 391, 369
 Kovács, G., Bakos, G. Á., & Noyes, R. W. 2005, MNRAS, 356, 557 (KBN)
 Kovács, G. & Bakos, G. Á. 2008, CoAst, 157, 82
 Kruszewski A., Semeniuk I. 2003, Acta Astr., 53, 241
 Mandushev, G., Torres, G., Latham, D. W. 2005, ApJ, 621, 1061
 Mazeh, T., Tamuz, O. & Zucker, S. 2007, ASP Conf. Ser., 366, 119
 Nagy, A. & Kovács, G. 2006, A&A, 454, 257
 Pont, F., Zucker, S., & Queloz, D. 2006, MNRAS, 373, 231
 Soszyński, I., Dziembowski, W. A., Udalski, A. et al. 2007, Acta Astron., 57, 201
 Soszyński, I., Poleski, R., Udalski, A. et al. 2008, Acta Astron., 58, 163
 Tamuz, O., Mazeh, T. & Zucker, S. 2005, MNRAS, 356, 1466
 Vilardell, F., Jordi, C. & Ribas, I. 2007, A&A, 473, 847

Appendix A: Unbiased estimation of the standard deviation of the residuals of least squares fits to sparsely sampled target functions

Here we derive a formula for the unbiased estimate of the standard deviation of the residuals when the target function is sparsely sampled relatively to the fitting functions of a Least Squares (LS) problem. This situation may occur in the case of the application of TFA, when we filter with a template set defined on a more extended time base than that of the target (a situation, that could be quite common in photometric databases containing data of diverse quality).

The LS problem is defined in the standard way

$$s^2 = \frac{1}{n} \sum_{i=1}^n \left[y(i) - \sum_{j=1}^m a_j x_j(i) \right]^2 = \min. \quad , \quad (\text{A.1})$$

where $\{y(i)\}$ is the target function (in the following: time series), $\{x_j(i); j = 1, 2, \dots, m\}$ are the fitting functions with the corresponding regression coefficients $\{a_j\}$. We note that the fitting functions might include any functions that contribute to the signal; for example, they might contain Fourier components and TFA templates. At the minimum variance, s stands for the root mean squares (RMS) of the residuals. Our assumptions are the following:

- All $\{x_j(i)\}$ are sampled in the same time base $\{t(i)\}$.
- The sampling time base \mathcal{T} of $\{y(i)\}$ is a nonzero subset of $\{t(i)\}$. This part of $\{y(i)\}$ contains n_1 data points.
- $\{y(i)\}$ is assumed to be zero-averaged by supplying “zeros” at the moments where it is not defined (in respect to $\{t(i)\}$).
- The noise $\{\eta(i)\}$ is additive in $\{y(i)\}$ with the following expectation values: $E(\eta(i)) = 0$, $E(\eta(i)\eta(j)) = \delta_{ij}\sigma^2$.
- The noiseless signal can be represented by the assumed model given by the best-fitting linear combination of $\{x_j(i)\}$.

With the above assumptions, the target time series reads as follows

$$y(i) = \begin{cases} 0 & \text{if } t(i) \notin \mathcal{T} \\ y_0(i) + \eta(i) - \langle y_0(i) + \eta(i) \rangle & \text{if } t(i) \in \mathcal{T} \end{cases}$$

Here $\langle y_0(i) + \eta(i) \rangle = \frac{1}{n_1} \sum_{i \in \mathcal{T}} [y_0(i) + \eta(i)]$, $\{y_0(i)\}$ is the noiseless part of the target function. With $g_{kl} = \sum_{i=1}^n x_k(i)x_l(i)$ and $b_k = \sum_{i=1}^n x_k(i)y(i)$ the solution of the LS problem reads as

$$a_j = \sum_{i=1}^m h_{ij} b_i \quad , \quad (\text{A.2})$$

where $\{h_{ij}\}$ is the inverse of $\{g_{ij}\}$ ($\sum_{j=1}^m h_{ij} g_{jk} = \delta_{ik}$). With these, the expectation value of the square of RMS can be written in the following form

$$E(s^2) = \frac{1}{n} \sum_{i=1}^n y^2(i) - \sum_{j,k=1}^m h_{jk} b_j b_k \quad . \quad (\text{A.3})$$

To compute the unbiased estimate of σ^2 , we need to evaluate the expectation value of s^2 . This is a straightforward computation, but we need to consider that the lack of data points in $\{y(i)\}$ as given above, will introduce extra correlation. Finally, we end up with the following expression

$$n \frac{E(s^2)}{\sigma^2} = n_1 - 1 - \sum_{j,k=1}^m h_{jk} (C_{jk} - S_j S_k) \quad , \quad (\text{A.4})$$

where $C_{jk} = \sum_{i \in \mathcal{T}} x_j(i)x_k(i)$ and $S_j = n_1^{-\frac{1}{2}} \sum_{i \in \mathcal{T}} x_j(i)$. It is easy to see that the above expression reduces to the familiar formula for the unbiased estimate of the variance if all items of the target function have matching time values with those of the fitting functions ($C_{jk} = g_{jk}$) and if the latter are also zero-averaged ($S_j = 0$).

Appendix B: Comments to the variable selection of Sect. 4

NOTES ON #1:

- 05021002-6850573 (SNR=33.1, Typ=RRc?) is a close companion of 05021018-6850566 (SNR=25.9, Typ=B?). Inspection of the LCs does not support an obvious blend scenario although their proximity strongly suggests that this is the case.
- 05022450-6850457 has features that may indicate that this is a $\sim 9 \text{ d}^{-1}$ (!) EB
- There are stars such as 05022832-6853097 with SNR=7.7 that have been omitted, because their LCs were ragged. In this particular case the alias components at $\sim 1 \text{ d}^{-1}$ are similarly strong, but we did not explore the possibility that this was the true frequency.
- Some of the red, short-periodic Misc candidates might actually be LPVs, but we cannot make a distinction, due to alias problems. For example, 05055618-6844166 was earlier classified as “Misc”, but: (i) the difference between the heights of the long- and the short-periodic peaks is less than 5%, (ii) the long-periodic LC indeed shows long-term features, (iii) the color is very red. So it is re-classified as “LPV”. The frequency and SNR given in Table 1 are those of the RAW analysis. Also, 05014177-6920207 has a frequency of nearly $\sim 1 \text{ d}^{-1}$. The frequency close to zero is also viable. The color is very red. Chances are that this is an LPV.

NOTES ON #79:

- Stars 05122749-6919426 and 05122739-6919434 are blends of each other. Since 05122749-6919426 has a slightly greater

SNR, we left this object as a variable in the database. However, this choice is not well justified. Only further observations with high resolution images can decide which one of these stars is the real source of the variation. SuperMACHO Project images go deeper and have better image quality and could resolve this ambiguity.

- 05123435-6904427: TFA yields a bit higher power at 1 d^{-1} alias. After visual inspection of the unfolded time series, we classified this variable as LPV.
- 05125486-6918537: The RAW light curve is noisy and ragged with a long shallow dimming in the first half of the observational time span. After TFA, the signal characteristics of $\text{SNR}=7.3$ and $f_{\text{peak}} = 1.00329 \text{ d}^{-1}$ did not seem to be convincing enough, to consider the variability as real.
- 05130892-6919317: Both RAW and TFA yield long periods, but it is actually aperiodic within the observational time span. Therefore, we assigned the RAW period and SNR to this star.
- 05161575-6926342: Some part of the long-term variation has been suppressed by TFA.
- 05162206-6925526: There is a relatively strong signal deformation by TFA but the LPV classification is secure.
- 05162318-6925457: is a heavily blended RRab (the three close companions are 05162314-6925413, 05162251-6925440 and 05162257-6925491).
- 05162865-6926167: TFA eliminates both the long-term drift and the short-term variation (approximately on a time scale of year with amplitudes of 0.05-0.1 mag). It is suspected that these variations are related to some systematics.
- 05162730-6926236: LPV (non-periodic). TFA yields a slightly higher peak at $\sim 1 \text{ d}^{-1}$, that could lead to a misclassification. Frequency, SNR entries are those of the RAW data.
- 05163808-6926589: TFA/BLS yields $\text{SNR}=7.7$, therefore, due to the SNR cutoff of ~ 9 employed on the BLS spectra, this star does not enter in our prime selection. Visual inspection of the LC folded by the BLS peak frequency of 0.5746619 d^{-1} might suggest an EB classification.

Table 1. Variable stars in the MACHO field # 1.

ID	V	V-R	$f[d^{-1}]$	SNR	Type	TFA
05011976–6921083	16.889	0.101	1.80367	14.5	B	1
05011992–6919188	17.585	0.049	0.37573	10.8	B	0
05011998–6917495	18.066	0.430	0.252205	16.9	EB	0
05012021–6920315	18.940	0.582	7.82853	7.0	d Sct?	1
05012029–6920248	19.615	0.113	0.02328	13.9	LPV	0

Notes:

- The object identification follows the notation of the 2MASS catalog, namely it is simply the abbreviated J2000 (RA,Dec) coordinates of the object. For example, 05011976–6921083 corresponds to RA=05:01:19.76, Dec=–69:21:08.3.
- The frequencies for type EB variables are given with larger number of digits, because of the higher sensitivity of the eclipse shape to the precision of the orbital period.
- The definition of the signal-to-noise ratio (SNR) and classification scheme are described in the text.
- Single digits under the column “TFA” mean exclusive TFA detections if “1” and pre-TFA detections if “0”.
- The excerpt shown is a part of the full table which is available only in the electronic version of this paper.

Table 2. Variable stars in the MACHO field # 79.

ID	V	V-R	$f[d^{-1}]$	SNR	Type	TFA
05122727–6920387	16.948	0.907	0.04885	8.9	LPV	1
05122740–6919308	16.270	0.091	1.31131	11.0	B	1
05122742–6903459	18.708	0.552	7.12253	7.2	d Sct	1
05122749–6919426	18.831	0.424	2.76320	26.5	RRab	0
05122754–6918475	18.626	0.046	0.47837	7.8	Misc	0

Note:

- See notes to Table 1.